RSC Advances

ROYAL SOCIETY OF CHEMISTRY

www.rsc.org/advances

Reassembling nanometric magnetic subunits into secondary nanostructures with controlled interparticle spacing

Koushik Saikia[1], Debasis Sen[2], Subhasish Mazumder[2] and Pritam Deb[1*]

[1]Advanced Functional Material Laboratory (AFML), Tezpur University (Central University), Tezpur, India
[2]Solid State Physics Division, Bhabha Atomic Research Centre, Mumbai 400085, India.
[*]Corresponding author's E-mail ID: pdeb@tezu.ernet.in

Abstract

Nanoparticle clusters have become attractive secondary nanostructures due to their collective physical properties, which can be modulated as the function of their internal structure. In this study, a reassembling strategy of iron oxide nanoparticles prior to the formation of nearly identical nanoclusters of size 80 ± 20 nm as the secondary nanostructures is reported, where ordered arrangement of nanoparticle subunits with narrow distribution of interparticle spacing is observed. Oleic acid capped iron oxide nanoparticles (IO_{NPs}@OA)with size 5 ± 2 nm are used as the primitive assembly of subunits. Post-functionalization of these nanoparticles with surfactant cetyltrimethyl ammonium bromide (CTAB) and subsequently with polyelectrolyte polyacrylic acid (PAA) result in irregular aggregation of nanoparticles (IO_{agg}@CTAB) and nanoparticle clusters (IO_{NPCs}@PAA) respectively. The orderly oriented carboxylate groups of PAA play the important role in dense packing of nanoparticles with ordered arrangement inside the clusters. The observed fractal morphologies give an indication of interparticle interactions for all three systems irrespective of assembly, aggregation and reassembly. Henkel plots show the dipolar type of interaction for all three systems. Dominant effect of interparticle spacing distribution over size on the modification of effective anisotropy energy barrier distribution is realized from the observed trend of ZFC (zero-field cooled magnetization) peak broadening and shifting.

Key words: reassembly, secondary nanostructures, interparticle spacing, small angle scattering, collective magnetic properties.

Introduction

Controlled assembly of magnetic nanoparticles as nanometric subunit into secondary nanostructures refers to an emerging bottom-up approach for constructing new functional systems, where the interparticle interaction can be modulated through the factors like spatial arrangement and interparticle spacing of the constituting nanoparticles.[1-4] Conversely, the strength of interparticle interaction (weak, strong and very-strong) controls the magnetic properties of such assemblies. For instance, large interparticle spacing results in very weak interactions, where nanoparticles behave as individual nanomagnets and which are suitable for high density recording media.[5] In contrast, close-packed assemblies result in collective properties due to strong interparticle interactions, which are of interest for efficient sensor fabrications.[5]

Properties of the magnetic nanoparticles are believed to be dependent directly on their sizes.[6-8] It is due to the modification of magnetic anisotropy energy with the size, which can even lead to the critical state like 'superparamagnetic state' below a particular size limit.[9, 10] In reality, it is not feasible to study the properties of a completely isolated magnetic nanoparticle. We can only deal with the assemblies of magnetic nanoparticles having different type of interparticle interactions, which can be of dipolar type or exchange type of interactions.[11] The study on the related magnetic properties for such assemblies is challenging because here both the size and interparticle interactions have to be taken into consideration. In this scenario, development of assembly of nanoparticles with narrow size distribution and well-defined morphologies is of prime importance to control efficiently their physical properties. Apart from different secondary self-assembly strategies, there are few established synthesis techniques, which can lead to *in-situ* formation of magnetic nanoparticles assemblies. Among these, thermal decomposition of organometallic complexes in presence of suitable capping agents,[12] polyol synthesis method,[13] co-precipitation of iron salts in highly basic medium[14] etc. are commonly used. Assembly structures achieved through these routes solely depend on the nature of the capping molecules and reaction parameters like temperature, pressure etc. However, the fundamental concern of these *in-situ* assemblies is retaining of similar size and morphologies of the nanoparticles with the variation of reaction parameters and the employed capping molecules.

In this aim, this work reports a novel strategy for the controlling of interparticle spacing during the formation of secondary nanostructures, keeping individual particle size, shape and phase identical. The process is achieved through an aggregation step followed by a reassembling step of iron oxide nanoparticles with the help of cationic surfactant CTAB and polyelectrolyte PAA. Polymer functional groups are utilized as the orderly oriented motifs, where positively charged CTAB functionalized nanoparticles are attached densely for resulting nanoparticle clusters. However, there are few reports on the clustering of iron oxide nanoparticles using polyelectrolyte-neutral block copolymers[15] and different hydrogels,[16] these methods are complicated and time consuming. In contrast, our reassembling based method is facile and cost effective for the preparation of nanoparticles clusters, where the strength of interparticle interaction and spatial arrangement play the important roles in determining the collective properties. The primitive assembly of iron oxide nanoparticles is prepared through *in-situ* capping with oleic acid, where interparticle spacing seems to be least. Along with the direct microscopic tool like high resolution transmission electron microscopy (HRTEM), the small angle x-ray scattering (SAXS) technique is employed to estimate the size and interparticle spacing distribution in the assembly state, aggregation state and finally in the reassembling state. Since, SAXS gives the overall structural informations unlike HRTEM, it is more appropriate to correlate the SAXS data to collective magnetic properties for a reliable structure-property correlation. The collective magnetic properties of all three systems are explained based on the observed variation in interparticle interaction related to the change in interparticle spacing. Moreover, the change in spatial arrangement of the nanoparticles in the aggregation and reassembling is directly related to the collective magnetic properties.

Experimental section

Materials

All chemicals were of analytical grade and used without further purifications. Iron sulphate ($FeSO_4.7H_2O$, 99%), tetramethylamonium hydroxide (TMAOH assay 25%), oleic acid ($C_{18}H_{34}O_2$, 90%), dimethylsulphoxide (DMSO, 99 %) and cetyltrimethyl ammonium bromide (CTAB, 99%) were procured from Merck. Polyacrylic acid (PAA, M_w = 1800) was procured from Sigma-Aldrich. Milli-Q water was used in all experiments.

Synthesis of oleic acid capped iron oxide nanoparticles (IO_{NPs}@OA)

The synthesis of oleic acid capped iron oxide nanoparticles was carried out using a modified protocol.[17] Here, 10 ml of aqueous solution containing 6 mmol $FeSO_4.7H_2O$ was first added into a three-necked round bottom flask with inert gas to remove oxygen followed by addition of 35 ml DMSO, 2 ml of oleic acid and 7 ml of TMAOH (*W/W* 25%). The mixture was stirred vigorously and subsequently refluxed at 140ºC for 30 minutes. Meanwhile, the solution colour gradually changed from orange to black. The flask was allowed to cool down to room temperature in ambient condition. The precipitates were obtained by magnetic separation and washed with ethanol three times. The collected precipitate was dried at 50°C in vacuum for 5 hrs.

CTAB functionalization for aggregation of iron oxide nanoparticles (IO_{agg}@CTAB)

7.5 mg of oleic acid capped iron oxide nanoparticles was dispersed in 0.5 ml of chloroform and added to 5 ml of aqueous solution containing 0.1 g of CTAB (0.274 mmol). The mixture was kept in vigorous stirring for 1 h and a homogenous oil-in-water microemulsion was obtained. After that the emulsion was heated at 60ºC for 10 minutes to evaporate chloroform from the solution which resulted in an aqueous phase dispersion of iron oxide nanoparticles. The aqueous solution was centrifuged at 7000 rpm for 15 minutes to precipitate down the nanoparticles. The precipitate was washed several times with equal volume of ethanol and water to remove the excess amount of CTAB and subsequently dried at 50ºC in vacuum for 5 hrs.

PAA mediated clustering iron oxide nanoparticles (IO_{NPCs}@PAA)

For PAA modification, 1.2 ml of PAA (1.2 *W/V*) solution was added drop wise to 5ml aqueous dispersion of CTAB functionalized nanoparticles with continuous stirring for 30 minutes. Then the resultant dispersion was centrifuged for 15 minutes at 7000 rpm to precipitate down the PAA modified nanoparticles and subsequently washed with equal volume of ethanol and water to remove unbound PAA. The washed product was dried at 50°C in vacuum for 5 hrs.

Analysis and characterizations techniques

Small angle scattering experiments were performed with the help of two techniques**,** small angle X-ray scattering (SAXS) and small angle neutron scattering (SANS) for knowing the structural information in two length scale ranges. SAXS of powder samples were carried out using a

laboratory based point collimation small angle scattering instrument. The scattered intensities $I(q)$ were recorded as a function of scattering vector transfer $q(= 4\pi \sin\theta/\lambda)$, 2θ being the scattering angle and λ the X-ray wavelength (λ = 0.154 nm). The intensities were corrected for sample absorption.[18] SANS experiments were carried out using a double crystal based medium resolution SANS (MSANS) instrument at the Guide Tube Laboratory of the Dhruva rector at Trombay, India.[19] The instrument consists of a non-dispersive (1, −1) setting of 111 reflections from a pair of single crystals with specimen between them. The scattered intensities have been recorded as a function of wave vector transfer similar to SAXS. The incident neutron wavelength for the present experimentwas 0.312 nm. The specimens under SANS investigations were placed on a sample holder with a circular slit of 1.5 cm diameter. The measured SANS profiles have been corrected for background and resolution effects.[18]

The crystalline phase of the nanoparticles were studied with Rigaku X-ray diffractometer (XRD) equipped with intense CuKα radiation (λ = 0.154 nm). The XRD data at room temperature were collected over a 2θ scattering range 10-70º with a step 0.05º. High resolution transmission electron microscopy (HRTEM) images were recorded on a JEOL 2100 electron microscope operating at an accelerating voltage of 200 kV. For this characterization, the colloidal solution of nanoparticles were deposited on to carbon coated grids and then dried at gentle temperature to evaporate the solvents. Statistical analysis was carried out with the help of the ImageJ software. For each sample, particle size distribution was calculated on about 200 nanoparticles from multiple images in bright field mode and fitted with a log-normal function

$$P(D) = \frac{A}{D\sigma\sqrt{2\pi}} exp\left[-\frac{(lnD - ln < D_{TEM} >)^2}{2\sigma^2}\right] \quad (1)$$

where, $< D_{TEM} >$ mean diameter, A area under fit and σ polydispersity of the distribution.

Atomic force microscopy (AFM) images of nanoparticles were recorded using Nanonics-AFM equipped with MultiView 1000 headinintermittent contact mode. An N-type Si probe with tip radius < 75 nm and resonance frequency 47-76 kHz was mounted to a standard silicon AFM tip mount. The scan was performed based on laser feedback mechanism with lower scanner movement. The Raman spectra of the samples were recorded using a Renishaw In-Via Raman spectrometer (Renishaw, UK) at a resolution of 0.3 cm^{-1}. Ar^+ laser of 514.5 nm wavelength is

used for excitation. The used laser power was 0.1 mW and passed through a 50X objective for illuminating the samples. Magnetic characterizations such as field dependent magnetizations (*M-H*) and temperature dependent magnetizations (*M-T*) were studied using a Quantum design Dynacool PPMS (Physical Property Measurement System) equipped with a vibrating sample magnetometer and superconducting coil which produces magnetic fields in the range of - 9T to+ 9T. Temperature dependent magnetizations were measured using ZFC (zero field cooling) and FC (field cooling) protocols. For ZFC, the sample was cooled in zero magnetic field from 300 K temperature to 10 K and subsequently magnetization was measured while warming the sample again to 300 K with a probe field 500 Oe. In contrast for FC, the sample was cooled in presence same probe field before measuring the magnetization with warming. For FC (*M-H*) measurement, the sample was cooled in presence of 5 T magnetic field to the measurement temperature (5 K) and then magnetization measurement was performed similar to normal *M-H*. The field dependence of remanent magnetization was measured using IRM (isothermal remanent magnetization) and DCD (direct current demagnetization) methods. For IRM, the sample was cooled to low temperature at zero field. After cooling, a small field was applied for 10 s, and then it was switched off and remanence was measured. The process was repeated with increasing magnitude of applied field up to 5 T. On the other hand, for DCD, after cooling the sample at zero magnetic field to low temperature, 5 T field was applied for 10 s, and then a small field was applied in the negative direction. After 10 s, it was switched off and the remanence was measured. The process was repeated with increasing field up to -5 T. Thermogravimetric analysis was carried out using a thermogravimetric analyzer (TGA, Perkin Elmer STA 6000). Measurements were performed in nitrogen atmosphere keeping the nitrogen flow rate of 20 ml $min^{-1}$and in the temperature range 50ºC-750ºC with heating rate 30ºC/min. The capping characteristics of the nanoparticles were characterized with Nicolet Fourier transforms infrared (FTIR) spectrometer. Zeta potential measurements were carried out with a Micrometritics NanoPlus zeta/nano particle analyzer.

Results and discussion

Assembly of Iron oxide nanoparticles

Iron oxide nanoparticles have been synthesized using a facile and simple method based on the oxidation of ferrous salt in a basic medium at moderate temperature 140°C. Oleic acid is

employed here as the *in-situ* capping agent to control the size and agglomeration of the nanoparticles. After proper washing and drying process, TEM characterization (Fig.1d and g) shows a uniform distribution of nearly spherical shaped nanoparticles with an average size 5 ±2 nm. The so-prepared nanoparticle system can be called as the *in-situ* assembly formation of iron oxide nanoparticles, where the interparticle spacing and hence interparticle interactions have been controlled through the steric repulsion among the capped nanoparticles. The effective oleic acid capping of the nanoparticles are confirmed from the FTIR and TGA results. FTIR spectrum (ESI1) shows the binding of oleic acid molecules to the nanoparticle surface through carboxylate group (COO^-) with chelating bidentate configuration, while the characteristic single step weight loss at the temperature range 200-450ºC in TGA (shown in Fig.2) confirms the monolayer capping of oleic acid over the nanoparticles.[20, 21]

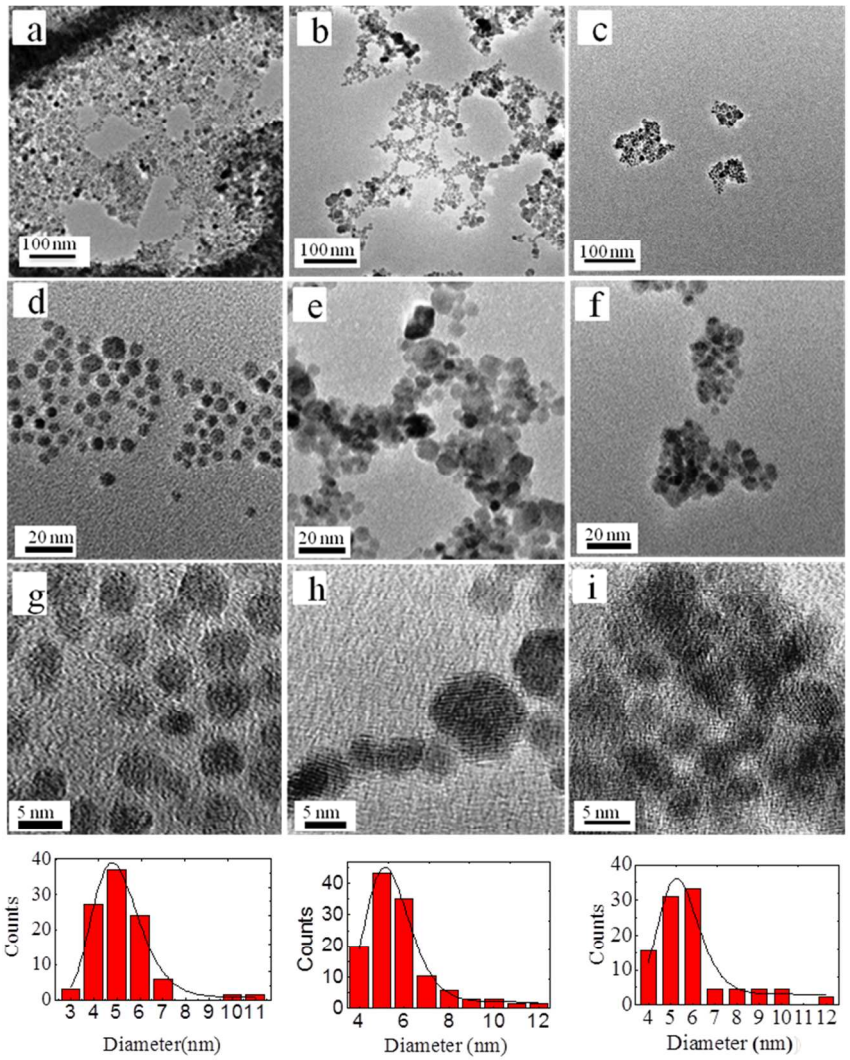

Fig.1 TEM images of (a) IO_{NPs}@OA, (b) IO_{agg}@CTAB and (c) IO_{NPCs}@PAA, (d-f) and (g-f) are their respective high resolution TEM images. Respective size distribution histograms are shown below.

Reassembling of iron oxide nanoparticles for clustering

Prior to the cluster formation from this assembly of hydrophobic nanoparticles, a two steps methodis followed. In the first step, the so-prepared nanoparticles are surface functionalized with a cationic surfactant CTAB for their phase transformation to hydrophilic phase using a simple microemulsion method. Here, oleic acid capped particles are dispersed in chloroform and subsequently mixed with the CTAB solution (CTAB in water) with vigorous stirring to form an oil-in-water emulsion. The obtained emulsion is heated at 60°C for the evaporation of chloroform, which ultimately results in the CTAB functionalized nanoparticles with hydrophilic phase. However, this phase transformation leads to the uncontrolled aggregation of the nanoparticles as observed from the TEM micrographs (shown in Fig.1b, e and h) and the AFM image (shown in Fig.3b). Trimodal and broad height distribution from the AFM image for the aggregate system stand for the non-uniformity of the aggregation morphology. The obtained aggregation is obvious, because, due to the strong hydrophobic-hydrophobic interaction through long carbon chains of oleic acid and CTAB, few oleic acid molecules can be detached from the nanoparticles surface during the functionalization. In addition, poor packing density of the remaining CTAB molecules over the nanoparticles cannot prevent the strong interparticle interaction. The removal of oleic acid capping from the nanoparticles is confirmed from the dramatic decrease of total weight loss percentage for the CTAB functionalized nanoparticles (~8.2 %) in comparison to oleic acid capped one (~14 %) (shown in Fig.2). Further, two stage weight loss steps for these CTAB functionalized nanoparticles (inset of Fig.2) imply two binding states of the CTAB molecules in the system. The first step weight loss (~6.56 %) at the temperature range 234-432°C might be due to the unbound or loosely bound CTAB molecule and the small step (~0.66 %) at 484-600°C may be resulted from the strong binding state of few CTAB molecules over the nanoparticles.[20]

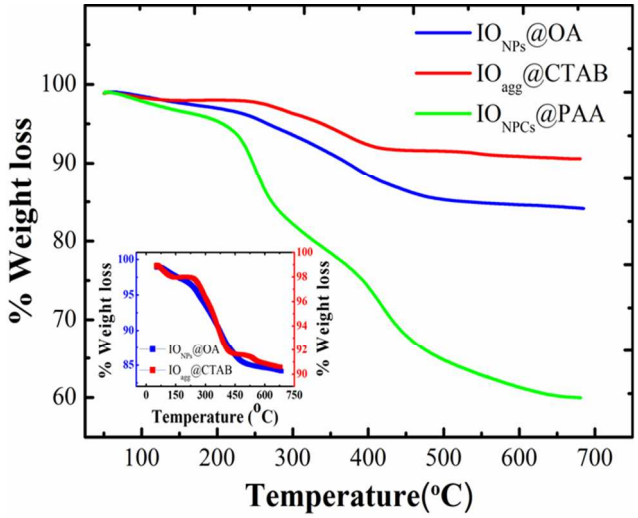

Fig.2 TGA weight loss comparison of IO_{NPs}@OA, (b) IO_{agg}@CTAB (c) IO_{NPCs}@PAA. Inset shows the comparison of first two samples in double y plot.

In the second step, these CTAB functionalized nanoparticles are further functionalized with electrolyte PAA to get the nanoparticle clusters. The idea is that, the cationic nature of polar head groups ($N^+(CH_3)_3$) of CTAB molecules over the nanoparticles might prefer the electrostatic binding with carboxylate group (COO^-) of PAA. The measured zeta potential for the so-prepared CTAB functionalized is +46 mV (ESI 2). In contrast, PAA solution (1.2 *W/V*) has shown negative value of zeta potential in the whole pH range 3.00 to 12.00. Based on the zeta potential results, the neutral pH (pH = 7.00) is identified as the optimized condition for effective PAA functionalization of the CTAB capped nanoparticles. The resultant solution of PAA functionalized nanoparticles has showed the zeta potential value + 27 mV. This decrement of the zeta potential could be due to the neutralization of some amount positive charges over the CTAB functionalized nanoparticles by negatively charged carboxylate groups of PAA, which is according to our expected mechanism. After washing for unbound PAA and drying, the PAA functionalized nanoparticles are re-dispersed in water for TEM and AFM characterizations. TEM shows distribution of nearly spherical shaped clusters of size 80 ± 20 nm with significant intercluster separation (shown in Fig.1c and f). AFM topography image also corroborates the TEM result as shown in the Fig.3c (shown in inset). Interestingly, the high magnification TEM micrograph shows a measurable interparticle spacing among nanoparticles inside the clusters (shown in Fig.1i), which is not observed for CTAB functionalized aggregate system (shown in Fig.1h). Since, through this functionalization process a measurable interparticle spacing has been regained similar to the primitive nanoparticles assembly, so, this functionalization step is termed

as the reassembling process. Moreover, the wrapping nature of the long chain polymer has resulted in the nearly spherical shape of the nanoparticle clusters with dense packing morphology. The dominant contribution of PAA in the cluster system is confirmed from the significant amount of weight loss (~39%) with characteristics two steps in TGA (shown in Fig.2). Based on the above observations, a model has been proposed for the said reassembling process as shown in the Scheme1. The model shows that, the negatively charged PAA carboxylate groups are functioning like orderly oriented motifs, where positively charged nanoparticles are bound to attach densely with a definite interparticle spacing due to strong electrostatic interaction.

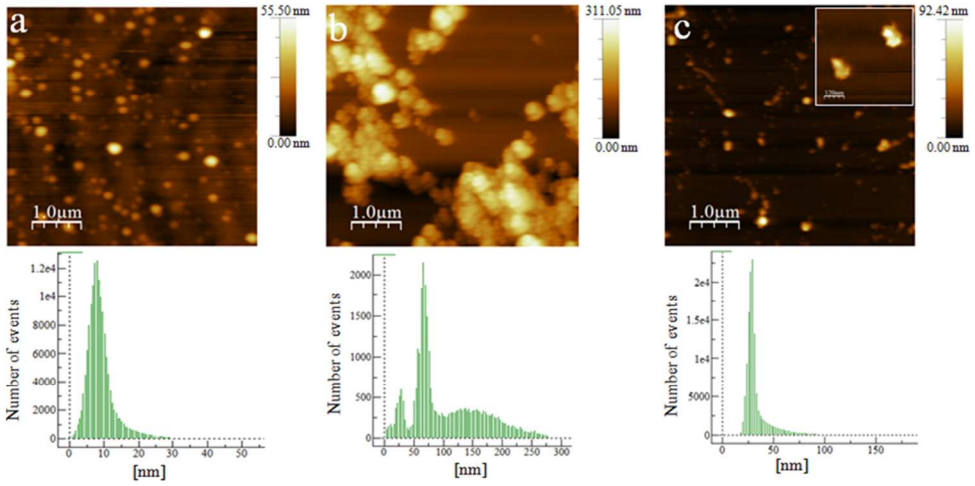

Fig.3 AFM height images of (a)IO_{NPs}@OA, (b) IO_{agg}@CTAB and (c) IO_{NPCs}@PAA with their respective height distributions. The inset in figure c shows two identical clusters (scale bar is 120 nm)

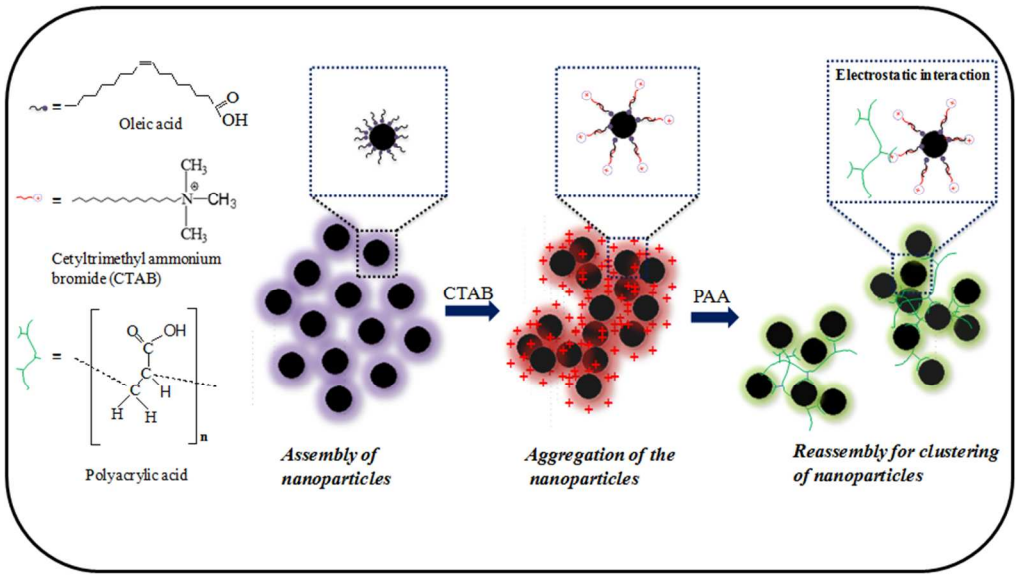

Scheme 1: Mechanism of reassembling of nanoparticles for cluster formation

Small angle scattering based structural investigations

To access the overall structural in-formations in the whole length scales ranging from individual nanoparticle dimension to the nanocluters size both SAXS and SANS have been used. In order to obtain the size distribution of the basic particles, the obtainedSAXS scattering intensity profile has been fitted with the scattering model of a polydisperse ensemble of interacting spherical particles. The observed intensity can be approximated [23] as

$$I(q) = C\left(\int_0^\infty \rho\,(R)R^6F^2(q,R)dR\right)S(q,R^{/}) \qquad (2)$$

where, C is the scale factor that depends on the scattering density contrast and the number density. $\rho(R)$represents the radial size distribution function, $F(q,R)$ is the form factor of a particle with radius $R$and$S(q,R^{/})$ represents the interparticle structure factor with the effective interparticle distance $2R^{/}$. The form factor $F(q,R)$of a spherical scatterer with radius R is given by

$$F(q,R) = 3[\sin(q\,R) - qRcos(qR)]/(qR)^3 \qquad (3)$$

The size distribution $\rho(R)dR$ represents the probability of finding a particle with radius R to $R + dR$ and has been assumed as log normal distribution function.

$$\rho(R) = \frac{1}{\sigma R\sqrt{2\pi}}exp\left[-\frac{\left(ln(R)-ln(\mu)\right)^2}{2\sigma^2}\right] \qquad (4)$$

where, σ and μ represent the polydispersity index and median of the radius distribution respectively.

The nature of the profile at low $q$regimeis determined by the nature of structure factor. For an attractive potential, the intensity at low q increases because of the formation of aggregated structure of the particles. In low q region of the SAXS profiles, the power law dependence of $I(q)$ on q (i.e., linear relation in double logarithmic scale) and with non-integer exponent of power law indicate fractal like morphologies in all the three systems, irrespective of assembling,

aggregation and reassembling. In reality, power law scattering is manifested in a limited q range determined by upper and lower cut-off lengths between which the system behaves as a fractal.[24, 25]

So, scattering curves are modelled using the form factor of a polydisperse spheres (subunit or monomer) and a mass fractal structure factor [26]

$$S(q, r_o) = 1 + \frac{D}{{r_o}^D} \int_0^\infty R^{D-3}\, h(r, \xi) \frac{\sin(qr)}{(qr)} r^2 dr \qquad (5)$$

with the fractal dimension, D, the radius of the monomer, r_o, the cut-off function $h(r,\xi)$ and ξ, cut-off length for fractal correlation. It has been found that, $S(q, R')$ corresponding to $h(r,\xi)$ of either, exponential cut-off or Gaussian cut-off represents well the present data,

Gaussian cut-off, $\quad h_{Gauss}(r, \xi) = exp\left[-\left(\frac{r}{\xi}\right)^2\right] \qquad (6)$

and exponential cut-off, $\; h_{Exp}(r, \xi) = exp\left[-\left(\frac{r}{\xi}\right)^1\right] \qquad (7)$

Fig.4a shows the transmission corrected scattered intensity profiles along with fitted curves. The fitted parameters such as fractal dimensions (D_m) of the systems and their basic subunit size (μ), polydispersity index (σ) and the approximate interparticle distance ($2r$) for all three systems are listed in the table 1. The SAXS curves for the IO_{NPs}@OA and IO_{NPCs}@PAA are fitted with two contributions; (i) basic nanoparticles with fractal morphology and (ii) a very small length scale (~ 2 nm) which could be due to oleic acid capping over the nanoparticles. Fig.4c shows the size distribution profiles of the subunits which is almost corroborating with the same obtained from TEM (size distribution histogram is shown in Fig.1). Also, the interparticle spacing measured from the high magnification TEM images are corroborating well with the SAXS results. It is worth mentioning here that the interparticle spacing distribution profiles are approximated from the average interparticle spacing and width of the particle size distribution obtained from SAXS. However, the slight dissimilarities in the trend of size distribution, polydisperty index and mean size can be attributed to the fact that the applied scattering tools are believed to give the overall structural informations about the system, while TEM provides the selective informations based on the region of interest. In this scenario, it will be more reliable for the explanation of magnetic

properties on the basis of structural information obtained from scattering data, as the measured magnetic properties arethe collective properties of the systems.

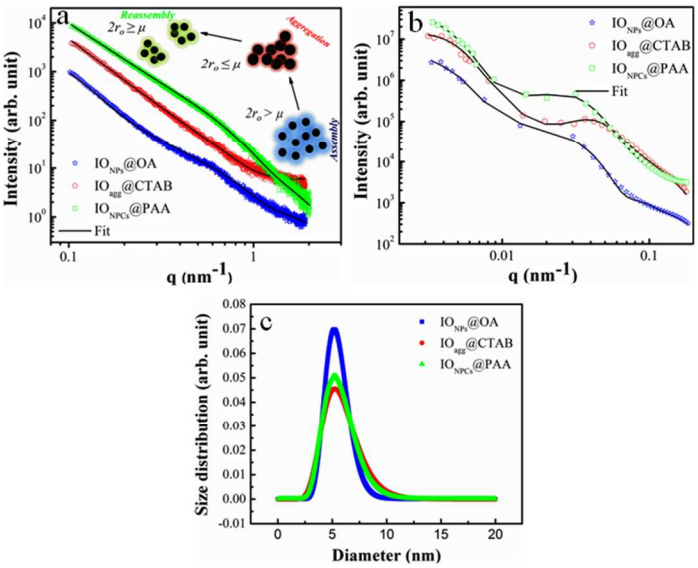

Fig.4 (a) SAXS and (b) SANS profiles in double logarithmic scale (Solid lines represent the fitted curves) (c) is the lognormal size distributions nanoparticles obtained from SAXS data.

System	Fractal dimension (D_m)	Median size (μ) of the NPs (nm)		Polydispersity index (σ)		Interparticle distance ($2r_o$) (nm)	
		HRTEM	SAXS	HRTEM	SAXS	HRTEM	SAXS
IO_{NPs}@OA	2.43 ± 0.01	5.0	5.40 ± 0.02	0.206	0.20 ± 0.01	6.3	5.8
IO_{agg}@CTAB	2.59 ± 0.01	5.3	5.68 ± 0.03	0.186	0.28 ± 0.01	4.9	4.8
IO_{NPCs}@PAA	2.39 ± 0.01	5.4	5.58 ± 0.02	0.169	0.26 ± 0.01	5.5	5.6

Table 1: Estimated structural parameters from SAXS and HRTEM.

For knowing the structural informations at larger length scale, SANS was employed for three systems of nanoparticles. Looking into the SANS intensity profiles (shown in Fig.4b) carefully, it is easily noticeable that SANS profiles of IO_{NPs}@OA and IO_{NPCs}@PAA are replicating each other in the region $q > 0.1$ nm^{-1}. In contrast, for the system IO_{agg}@CTAB, it is deviated slightly in the intermediate q range (0.01-0.05 nm^{-1}). These observations can be related to the reassembly mediated regaining of the overall system structure at larger length scale. Table shown in ESI 3 gives the obtained length scales from SANS data, which are corroborating with the TEM results. However, interaction at these larger length scales may be ignored here for its correlation with magnetic properties.

Structural phase of nanoparticles

Proper identification of the structural phase of the iron oxide nanoparticles in all the three systems is very important, as the structural phase is directly related to the ground state magnetic properties of the nanoparticles. XRD result shows the maghemite phase (γ-Fe_2O_3) of the oleic acid capped iron oxide nanoparticles (ESI4). However, the Raman spectra show the presence of both maghemite and magnetite (Fe_3O_4) phases for the nanoparticles in all three systems. Since the used laser power in Raman characterization was extremely less (0.1mW) and the exposure time was very short, the possibility of laser induced phase transformation can be avoided here. Supporting the Raman results FTIR spectra also show the signature of both magnetite and maghemite phases of the iron oxide nanoparticles (shown in ESI 5). The observed bi-phasic composition could be due to the unwanted surface oxidation of the magnetite nanoparticles.[27] The difference in the result of XRD and spectroscopic techniques (Raman and FTIR) may be realized by the fact that the diffraction maxima for maghemite and magnetite (same cubic inverse spinel structure) are in close proximity and for nanosystems the broadened peaks overlap sometimes. Hence, it becomes difficult from XRD to distinguish them. However, the spectroscopic technique, especially, Raman spectroscopy is very sensitive in discrimination of the phases. Cubic inverse spinel structure belongs to the space group $O_h^7(Fd3m)$, for which group theory predicts the following modes [28, 29]

$$\Gamma = A_{1g} + E_g + 3T_{2g} + T_{1g} + 2A_{2u} + 2E_u + 5T_{1u} + 2T_{2u} \quad (8)$$

where, the first five modes are Raman active and rest of the modes are IR active. Magnetite exhibits all five Raman modes: A_{1g} ~670 rcm^{-1},[30] E_g ~ 306 rcm^{-1} [30] and three T_{2g} ~193 rcm^{-1},[30] 490 rcm^{-1} [31] and 570 rcm^{-1} [30] while for maghemite four Raman modes are reported, namely, E_g ~ 350 rcm^{-1}, T_{2g} ~500 rcm^{-1}and un-resolved A_{1g} modes at 678 rcm^{-1}and 710 rcm^{-1}.[29]

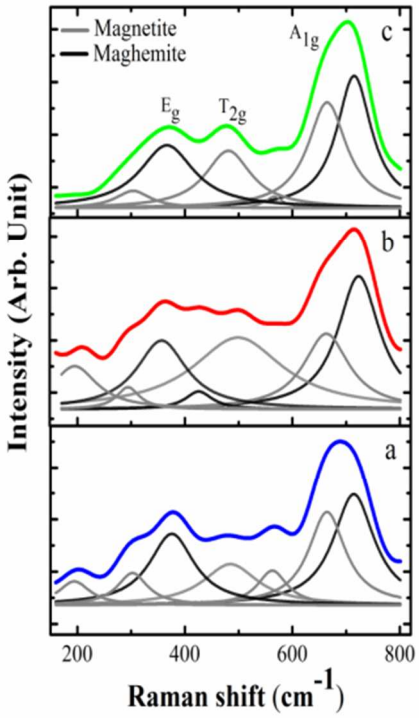

Fig.5 Raman spectra comparison of (a) IO_{NPs}@OA, (b) IO_{agg}@CTAB and (c) IO_{NPCs}@PAA, where, Lorentzian deconvolutions show positions of magnetite and maghemite phases.

Fig.5a-c show the Raman spectra of these three systems of nanoparticles taken in ambient conditions, where the characteristics bands of both magnetite and maghemite phases are observed. The deconvolution of different bands has been achieved by fitting the spectra with Lorentzian profile. The positions and assignments of all bands are listed in table (ESI6). Thus, from the Raman and FTIR results a core-shell structure (predominant magnetite phase) of the constituent nanoparticles can be assumed, considering a thin maghemite shell formed due to the symmetric surface oxidation.

Collective magnetic properties

Retaining the structural phase, size and shape of the individual nanoparticle during the aggregation and reassembling steps may help in the explanation of the collective magnetic

properties in terms of interparticle interactions. Field dependent magnetization (*M-H*) and temperature dependent magnetization (*M-T*) studies have been carried out to have an insight to the effect of interparticle interaction on the collective magnetic properties. Fig.6 shows the comparative *M-H* plots of the three systems. The characteristics of the room temperature *M-H* plots, like negligible values of coercivity (H_c) and reduced remanence (M_r/M_s) give the indication of superparamagnetic property of nanoparticles in all three systems.[32,33] However, the intricate physics inherent in the observed magnetic behaviours have been known only after proper estimation of these parameters along with the saturation magnetizations (M_s). Magnetization values are corrected with TGA total weight losses and shown in the Table 2 along with the coercivities and remanances. It is observed that the cluster system shows the highest M_s value, while the first two systems show almost similar values. The observation is same at low temperature (5 K) also, however, the difference is less. The enhancement in M_s may be due to stronger interparticle interaction in the cluster system. Similar enhancement in M_s for iron oxide nanoparticle cluster was reported, where, a versatile diblock copolymer was employed for cluster formation.[34] For knowing the type of interaction and comparative interaction strength, isothermal remanent magnetization and (IRM) and direct current demagnetization (DCD) measurements have been done. Henkel plots obtained from these measurements have confirmed the presence of dipolar interaction (negative value of δM) in all three systems (shown in the Fig.7). It is observed maximum for the IO_{NPCs}@PAA sample and minimum for the IO_{NPs}@OA. Due to the demagnetizing effect of dipolar interaction it is usual that system with stronger dipolar interaction should give lower value of coercivity compared to the moderate interaction strength.[35, 36] Therefore, in the case of IO_{NPCs}@PAA sample the lowest coercivity is obtained. However, the same is not observed for IO_{agg}@CTAB sample, as it should show lower coercivity compared to the first sample (IO_{NPs}@OA). The observed maximum coercivity for this system can be related to the partial orientation of magnetization easy axis of the nanoparticles in the aggregated system, where, strengthening of dipolar interaction behaves oppositely, hence enhances the coercivity and remanence.[37] It is worth mentioning here that for the cluster system though comparatively higher ordered arrangement of the nanoparticles have been obtained, but the orientation of easy magnetization axes are randomly textured. Again, like corecivity changes the similar trend is not followed by the changes in remanence values in three cases. Though, for the aggregate system the remanence is obtained maximum, the cluster system has not shown its

value minimum. Thus, it can be concluded that the dipolar interaction and the spatial orientation of easy axis act in competitive manner for modifying coercivity and remanence of the nanoparticle systems.

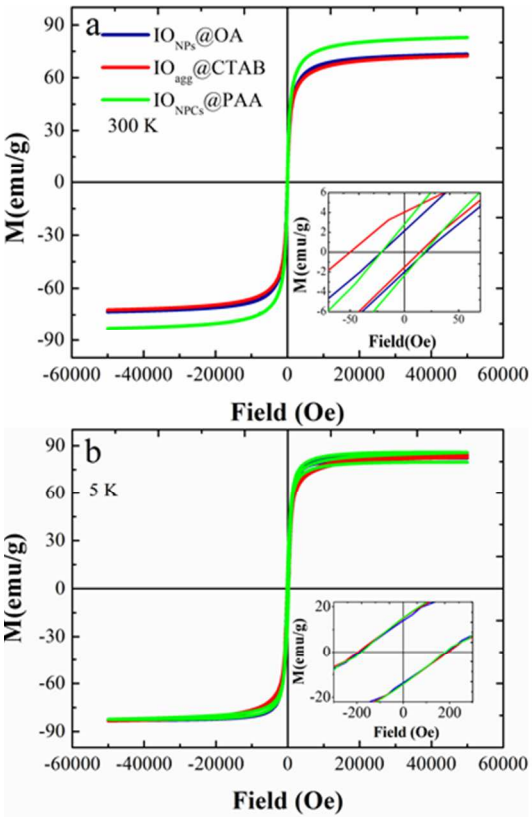

Fig. 6 TGA corrected M-H plots of IO_{NPs}@OA, IO_{agg}@CTAB and IO_{NPCs}@PAA at 300K (a) and 5K (b).Insets show magnifications of M-H plots for H_c and M_r measurements.

The thickness of magnetic dead layers (D_L) has been calculated for the three systems using the equation (9).[38]

$$M_{So} = M_S^{bulk}\left(\frac{d/2 - D_L}{d/2}\right)^3 \qquad (9)$$

Here, M_{So} is the TGA corrected saturation magnetization value, M_S^{bulk} is the bulk magnetization value of the material and 'd' is the nanoparticle diameter. Based on the earlier structural analysis,

it is assumed that the predominant magnetite phase is retained in all three systems. Therefore, M_S^{bulk} is taken as 92 emu/g,which is the bulk magnetization value of magnetite.[39]

Interestingly, for the IO_{NPs}@OA and IO_{agg}@CTAB the dead layer thickness are obtained almost same (~ 0.2 nm) and for the third system it is obtained significantly less (~ 0.1 nm) as shown in the table 2. It is worth mentioning that like the first two systems TGA corrected M_s value (82.36 emu/g) of IO_{NPCs}@PAA is found not much lesser than the bulk magnetite M_s (92 emu/g). Ideally, it should not be significantly higher in comparison to the earlier two systems, because same initial iron oxide nanoparticles were used. If it would have been found significantly smaller, the explanation could be given as: two steps functionalization might be responsible for this decrement. In this situation, the only reason that can be responsible for the observed enhancement of *Ms* is the enhanced interparticle interaction in the cluster system. However, it cannot be ignored that, for the calculation of the dead layer thickness the collective magnetization (M_s) values (after TGA correction) have been used, which are already affected by the interparticle interaction.

Sample	Total weight loss (%)[a]	M_s(emu/g)[b]		H_c(Oe)		(M_r/M_s)[c]		Dead layer thickness D_L(nm)
		300 K	5 K	300 K	5 K	300 K	5 K	
IO_{NPs}@OA	14.0	73.13	83.45	20.05	188.43	0.02	0.16	0.20
IO_{agg}@CTAB	8.2	72.48	84.30	35.57	196.88	0.04	0.17	0.21
IO_{NPCs}@PAA	39.0	82.36	86.24	19.41	181.20	0.03	0.17	1.08

[a] Total weight loss determined by TGA, [b]corrected saturation magnetization values using TGA weight losses and [c] reduced remanence

Table 2: Paramters obtained from *M-H* measurements and TGA data.

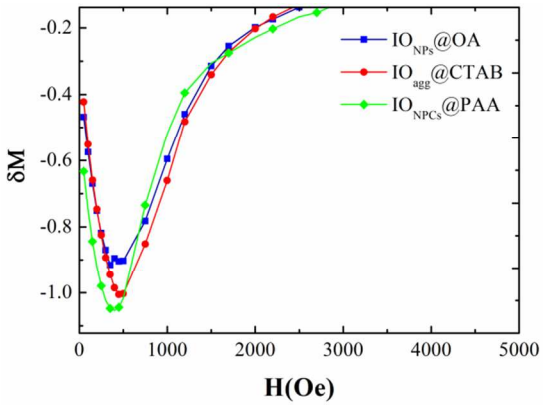

Fig. 7 Measured Henkel plots for the three systems

The blocking phenomenon of the magnetic moments and its dependency on the interparticle interaction have been studied with ZFC (zero field cooled) and FC (field cooled) magnetization measurements as shown in the Fig.8a-c. ZFC and FC curves show the distinct features like broad ZFC peaks with maxima T_{max} and that the ZFC and FC coincide at high temperatures but split at a temperature T_{irr} (irreversible temperature) for all three systems. For non-interacting magnetic nanoparticles, T_{max} is directly proportional to the average blocking temperature $<T_B>$ through $T_{\max} = \beta < T_B >$ (where, β is the proportionality constant depending on the type of size distribution in the order of 1.5 to 2.0[40]) marks a crossover region where average anisotropy barrier energy and the energy caused by thermal energy (k_BT) are comparable. When the anisotropy energy is predominant (for $T < T_{max}$) it is blocked state and for its opposite ($T > T_{\max}$) the superparamegntic state starts. Generally, for a particle of volume V, blocking temperature T_B is defined as the temperature at which relaxation time described by the Neel relaxation time $\tau = \tau_{\circ}\exp\left(\frac{E_B}{k_BT}\right)$, where the anisotropy energy barrier height $E_B = KV$, becomes equal to the measuring time t_m.T_{irr} signifies the highest blocking temperature, i.e. at this temperature the relaxation time of the biggest particle in the assembly is comparable to the measurement timet_m.[41]Thus, both T_B and T_{irr} are distribution dependent parameters and the difference between T_{max} and T_{irr} is bound to provide a qualitative width of the energy barrier distribution related to the distribution of particle size. In absence of any broad size distribution the only factor that can affect these parameters significantly is the interparticle interactions. In fact, the SAXS results show narrow and similar size distribution profile of nanoparticles in all three systems (Fig.4c). So, the observed broadening and separation between T_{irr} and T_{max} could be related to modification of energy barrier distribution due to enhanced interparticle interactions in the aggregated and cluster systems. The approximate interparticle distance distributions obtained from SAXS results are corroborating with the trend of ZFC peak broadening for the three systems as shown in the Fig.8 a-d. This implies the significant role of interparticle spacing distribution for the modification of energy barrier distribution. Another noticeable observation is the up-shifting of T_{max} for the aggregated and the cluster systems, which again signifies the enhanced interparticle interaction. This type of behaviours such as ZFC broadening and higher temperature shifting of average blocking temperature $<T_B>$ and hence T_{max} due to enhanced

interparticle interaction with increasing concentration of magnetic nanoparticles were observed in both experimental and simulation studies.[42,43] Interestingly, here the up-shift for IO_{agg}@CTAB was observed maximum (~ 88K), while for IO_{NPCs}@PAA it was reverted back (~ 24 K). This can be correlated to the influence of dipolar interaction due to the change in interparticle spacing for aggregation and cluster systems. When particles are in direct contact (i.e, $2r_o \leq \mu$) for aggregation system, the T_{max} is shifted to higher temperature and again it is reverted back for the cluster system, where a measured interparticle spacing is obtained (i.e, $2r_o \geq \mu$). For the IO_{NPCs}@PAA system, the increased separation among the nanoparticles due to their oriented binding to the polymer carboxylate group should result for intermediate dipolar strength. However, the Henkel plots show its value maximum for this system. The obtained strongest dipolar strength could be resulted from the comparatively more random orientation of magnetization easy axis as explained in earlier discussion. The retaining of similar overall shape of all ZFC curves irrespective of the assembly type nullifies the possibility of any percolation during cluster formation, because above the percolation limit ZFC curves show some distinctive shape due to the formation of coherent ferromagnetic clusters.[44] Moreover, the possibility of the formation of any superspin-glass state among the nanoparticles after aggregation and clustering is discarded from the observed monotonic decrement of FC magnetizations with increase of temperature below T_{max}. Because, for spin-glasses, FC curves show some plateau like feature below T_{max}.[45]

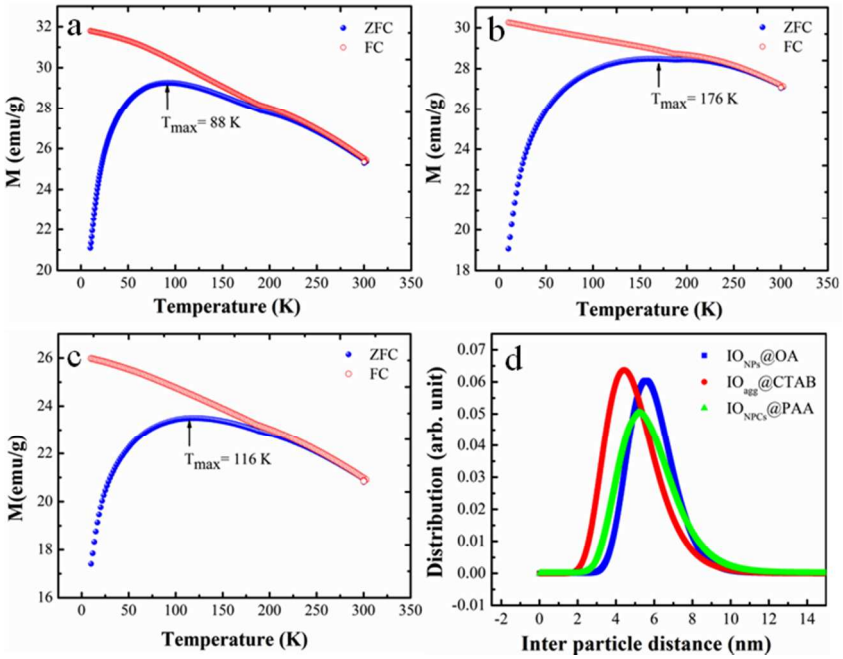

Fig.8 ZFC and FC curves of (a) IO_{NPs}@OA, (b) IO_{agg}@CTAB and (c) IO_{NPCs}@PAA with the probe field 500 Oe. (d) shows the interparticle distance distribution profiles of nanoparticles for these three systems obtained from SAXS analysis.

Another noticeable feature in the ZFC and FC curves is the appearance of a kink in the irreversible region above the T_{max} and the position of which is almost same for all three systems. This type of kink may be correlated to the difference in spin states of core and shell in a core-shell composite. Here, the core-shell nanoparticle is of ferrimagnetic magnetite core and ferrimagnetic maghmetite shell. Maghemite shell is assumed to be formed due to symmetric surface oxidation of smaller size magnetite nanoparticles. It is known that FC and ZFC magnetization curves of strongly exchange coupled core-shell system do not show separate signature as the spins of their core and shell are strongly correlated, however, core-shell systems with weak spin coupling at the interface can exhibit some features. Thus, the observed kink in M-T is not unusual, as in our core-shell nanoparticles there should not be strong exchange coupling. The weak exchange coupling is confirmed from the zero exchange bias effect in all three systems as shown in the Fig.9. Similar kink feature in M-T measurement was reported for Fe_3O_4/γ-Mn_3O_4 core-shell system also, where the presence of weak exchange coupling was justified with zero exchange bias effect.[46]

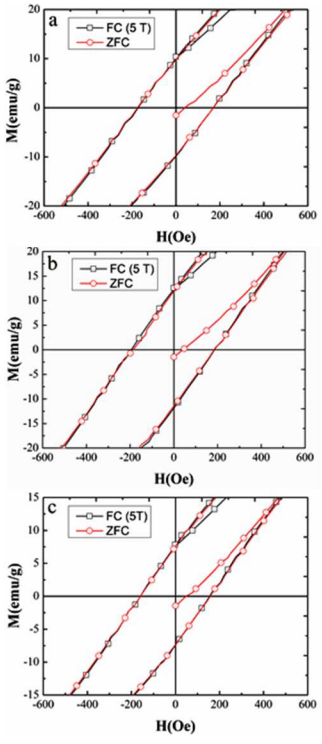

Fig.9. M-H at FC and ZFC conditions taken at temperature 5 K.

Conclusions

In summary, we have reported a novel strategy of reassemblingmagnetite nanoparticles for achieving nearly spherical nanoclusters as the secondary nanostructures. As the primitive system, an assembly of oleic acid capped nanoparticles with uniform distribution and sufficient interparticle spacing are obtained through an *in-situ* capping route. Two steps functionalization with CTAB and subsequently with PAA result in desired nanoclusters. The second phase functionalization is realized as the mentioned reassembling process,becausehere individual nanoparticles are found to be orderly arranged state with narrow distribution of interparticles spacing similar to the primitive assembly. Oriented electrostatic binding between positively charged CTAB capped nanoparticles and carboxylate group of PAA is found to be reasonable for this ordering state. The self-similarity of individual subunit or iron oxide nanoparticles in all three systems is ensured from the similar fractal characteristics. The collective magnetic properties are found solely dependent on the structural degree of freedom of nanoparticles in all the three systems. The significant role of dipolar interaction in modulation of the collective magnetic properties is understood on the basis of altered spatial arrangement of nanoparticles, while transforming from assembly to reassembly state via intermediate aggregation state. The dominant effect of interparticle spacing over size distribution of the nanoparticles is inferred from the observed trend of ZFC peak broadening in temperature dependent magnetization measurment. The obtained secondary nanostructures with controlled spatial arrangement will have potential in wide technological applications with improved efficiency.

Acknowledgement

The authors acknowledge the UGC-DAE-CSR, Mumbai Centre, India, forproviding financial support vide grant no. UDCSR/MUM/AO/CRS-M-186/12/508. The authorsalso gratefully acknowledge SAIF, NEHU for providing the access to the transmission electron microscopy. KS would like to acknowledge Mr. Pawan Chetri for his help with the Raman spectroscopy.

Notes and references

1. D. Toulemon , B. P. Pichon,C. Leuvrey,S. Zafeiratos,V. Papaefthimiou, X. Cattoenand S.Begin–Colin,*Chem. Mater.,*2013, **25**, 2849.
2. S. Singamaneni, V. N. Bliznyuk, C. Binekc and E. Y. Tsymbal, *J. Mater. Chem.*, 2011, **21**, 16819.
3. V. Russier, C. Petit, J. Legrand and M. P. Pileni, *Phys. Rev. B,* 2000,**62**, 3910.
4. H. T. Yang, D. Hasegawa, M. Takahashi and T. Ogawa, *Appl. Phys. Lett.,* 2009, **94**, 013103.
5. B. P.Pichon, C. Leuvey, D. Ihawakrim, P. Bernard, G. Schmerber and S. Begin-Colin, *J. Phys. Chem. C,* 2014, **118**, 3828.
6. A. Demortiere, P. Panissod, B. P. Pichon,G. Pourroy, D. Guillon, B. Donnio and S. Begin-Colin, *Nanoscale,* 2011, **3**, 225.
7. P. Guardia, A. Labarta and X. Batlle, *J. Phys. Chem. C,* 2011, **115**, 390.
8. D. Kechrakos and K. N. Trohidou, *J. Magn. Magn. Mater*., 2003, **262**, 107.
9. A. H. Lu, E. L.Salabas andF. Schuth, *Angew. Chem. Int. Ed.,*2007, **46**, 1222.
10. C. Liu, B. Zou, A. J. Rondinone and Z. J. Zhang, *J. Am. Chem. Soc.,*2000, **122**, 6263.
11. S. Morup, M. F. Hansen and C. Frandsen, *Beilstein J. Nanotechnol.,* 2010, **1**, 182.
12. D. K. Jha, M. Shameem, A. B. Patel, A. Kostka, P. Schneider, A. Erbe and P. Deb, *Mater. Lett.,* 2013, **95**,186.
13. C. Cheng, F. Xua and H. Gu, *New J. Chem.,* 2011, **35**, 1072.
14. M. C. Mascolo, Y. Pei andT. A. Ring, *Materials,*2013, **6**, 5549.
15. Jean-Francois Berret, N. Schonbeck, F. Gazeau, D. E. Kharrat, O. Sandre, A. Vacher and M. Airiau, *J. Am. Chem. Soc.,* 2006, **128**, 1755.
16. C. Paquet, H. W. de Haan, D. M. Leek, Hung-Yu Lin, B. Xiang, G.Tian, A. Kell and B. Simard, *ACS Nano*, 2011, **5**, 3104.
17. C. Y. Wanga, J. M. Hong, G. Chene, Y. Zhanga and G. Ning, *Chin. Chem. Lett.,* 2010, **21**,

179.

18. P. W. Schmidt and R. Height, *Acta Cryst.,* 1960, **13**, 480.

19. S. Mazumder, D. Sen, T. Sarvanan and P.R. Vijayraghavan, *J. Neutron Res.,* 2001*,* **9**, 39.

20. A. G. Roca, M. P. Morales, K. O.Gradyand C. J. Serna, *Nanotechnology,* 2006, **17**, 2783.

21. P. Dallas, N. Moutis, N.E. Devlin, D. Niarchos and D. Petridis, *Nanotechnology,* 2006, **17**, 5019.

22. S. H. Wu and D. H. Chen, *J. Colloid Interface Sci.,* 2004, **273**, 165.

23. J. S. Pedersen and I. W. Hamley, *J. Appl. Cryst*., 1994, **27**, 36.

24. J. Teixeira, *J. Appl.Cryst.,* 1988, **21**, 781.

25. T. Freltoft, J. K. Kjems and S.K. Sinha, *Phy. Rev. B,* 1986, **33**, 269.

26. N. Mahmoudi, M. A. V.Axelosb andA. Riaublanc, *Soft Matter,* 2011, **7**, 7643.

27. R. L. Rebodos and P. J.Vikesland, *Langmuir,* 2010, **26**, 16745.

28. L. Stagi, J. A. D. Toro,A. Ardu, C. Cannas,A. Casu,S. S. Lee and P. C.Ricci, *J. Phys. Chem. C,* 2014, **118**, 2857.

29. A. M. Jubb and H. C. Allen, *ACS Appl. Mater. Interfaces.,* 2010,**2**, 2804.

30. L. V. Gasparov, D. B. Tanner, D. B. Romero, H. Berger, G. Margaritondo and L. Forro, *Phys. Rev. B,* 2000, **62**, 7939.

31. P. R. Graves, C. Johnston and J. J. Campaniello, *Mater. Res. Bull.,*1988, **23**, 1651.

32. M. Mahmoudi, A. Simchi, M. Imani, A. S.Milani andP. Stroeve, *J. Phys. Chem. B,*2008, **112**, 14470.

33. M. Mahmoudi, A. Simchia, M. Imanic, M. A. Shokrgozard, A. S. Milanie, U. O. Hafelif and P. Stroeveg, *Colloids Surf. B,* 2010, **75**, 300.

34. H. Chen, J. Yeh, L. Wang, H. Khurshid, N. Peng, A. Y. Wang and H. Mao, *Nano Res.,* 2010, **3**, 852.

35. D. Kechrakos and K. N. Trohidou, *Phys. Rev. B*, 1998, **58,** 12169.

36. A. F. Gross, M. R. Diehl, K. C. Beverly, E.K. Richman and S. H. Tolbert, *J. Phys. Chem. B,* 2003, **107**, 5475.

37. A. T. Ngo and M. P. Pileni, *J. Phys. Chem. B,* 2001, **105**, 53.

38. C. Pereira, A. M. Pereira, C. Fernandes, M. Rocha, R. Mendes, M. P. Fernández-García, A. Guedes, P. B. Tavares, Jean-Marc Grenèche, J. P. Araújo and C. Freire, *Chem. Mater.,* 2012, **24**, 1496.

39. W. Wu, X. Xiao, S. Zhang,H. Li, X. Zhou and C. Jiang, *Nanoscale Res. Lett,*2009,**4**,926.

40. D. Peddis, F. Orrù, A. Ardu, C. Cannas, A. Musinu andG. Piccaluga,*Chem. Mater.,* 2012, **24**, 1062.

41. P. Dey, T. K. Nath, P. K.Manna andS. M. Yusuf, *J. Appl. Phys,*2008,**104**, 103907.

42. G. Margaris, K. N. Trohidou, V. Iannotti, V.G. Ausanio, L. Lanotte and D. Fiorani, *Phys. Rev. B,* 2012, **86**, 214425.

43. K. Nadeem, H. Krenn, T. Traussnig, R. Wurschum, D.V. Szabo and I. Letofsky-Papst, *J. Magn. Magn. Mater*. 2011, **323**, 1998.

44. J. M. Vargas, W. C.Nunes, L. M. Socolovsky, M. Knobel and D. Zanchet, *Phys. Rev. B,* 2005*,* **72**, 184428.

45. S. Thomas, M. Uhlig, U. Wiedwald, L. Han, P. Ziemann and M. Albrecht, *Nanotechnology,* 2013*,* **24,** 155703.

46. P. K. Manna andS. M.Yusuf, *J. Phys. D: Appl. Phys.,* 2011, **23**, 506004.

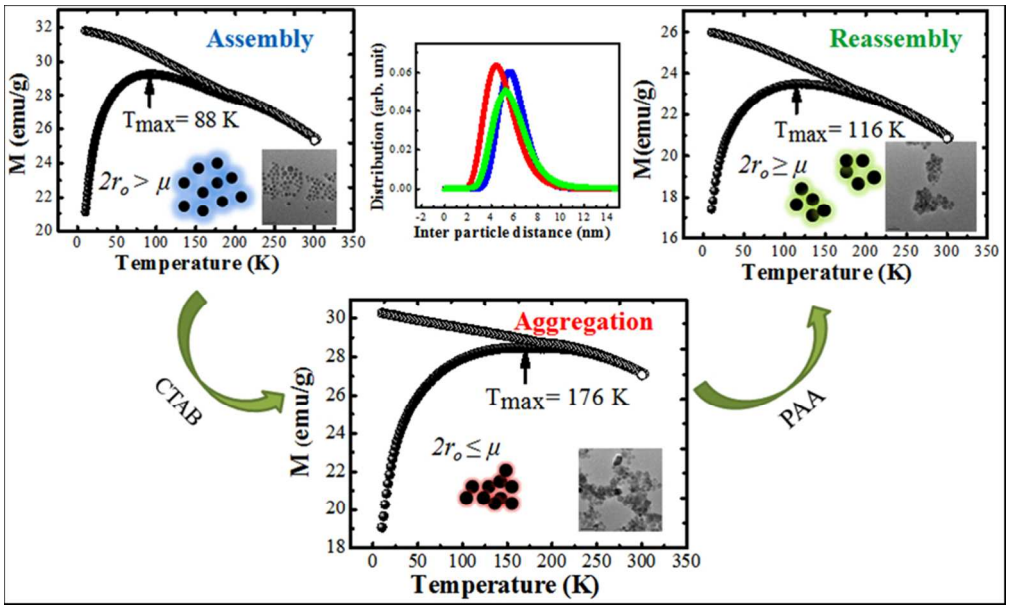

201x120mm (115 x 115 DPI)